



Article

Seasonal Variation in Microphysical Characteristics of Precipitation at the Entrance of Water Vapor Channel in Yarlung Zangbo Grand Canyon

Ran Li, Gaili Wang *, Renran Zhou, Jingyi Zhang and Liping Liu

State Key Laboratory of Severe Weather, Chinese Academy of Meteorological Science, Beijing 100081, China; liran201@mailsucas.ac.cn (R.L.); zhoudenran21@mailsucas.ac.cn (R.Z.); 3190101053@stu.cuit.edu.cn (J.Z.); liulp@cma.gov.cn (L.L.)

* Correspondence: wanggl@cma.gov.cn

Abstract: Mêdog is located at the entrance of the water vapor channel in the Yarlung Zangbo Grand Canyon (YGC). This area has the largest annual accumulated rainfall totals and precipitation frequency on the Tibetan Plateau (TP). This paper investigates the seasonal variation in raindrop size distribution (DSD) characteristics in Mêdog based on disdrometer observations from 1 July 2019 to 30 June 2020. The DSD characteristics are examined under six rain rate classes and two rainfall types (stratiform and convective) in the winter, premonsoon, monsoon and postmonsoon periods. The highest (lowest) concentration of small raindrops is observed in monsoon (winter) precipitation, whereas large raindrops predominate in premonsoon precipitation. For stratiform rainfall, the mean mass-weighted mean diameter (D_m) exhibits overlooked differences in the four periods, while the mean normalized intercept parameter (N_w) is significantly higher in the monsoon period than in the other three periods. The convective rainfall in the monsoon and postmonsoon periods is characterized by a high concentration of limited-size drops and can be classified as maritime-like. This is probably attributed to abundant warm and humid airflow transported by the Indian Ocean monsoon into Mêdog. The westerly winds prevail over the TP during the premonsoon period, and thereby the premonsoon convective rainfall in Mêdog has a larger mean D_m and a lower mean N_w . In addition, the relationships of radar reflectivity Z and rain rate R for different precipitation types in different periods are also derived. A better understanding of the seasonal variation in the microphysical characteristics of precipitation in Mêdog is important for improving the microphysical parameterization scheme and the precipitation forecast of models on the TP.

Keywords: Tibetan Plateau; raindrop size distribution (DSD); seasonal variation; maritime-like



Citation: Li, R.; Wang, G.; Zhou, R.; Zhang, J.; Liu, L. Seasonal Variation in Microphysical Characteristics of Precipitation at the Entrance of Water Vapor Channel in Yarlung Zangbo Grand Canyon. *Remote Sens.* **2022**, *14*, 3149. <https://doi.org/10.3390/rs14133149>

Academic Editor: Federico Porcù

Received: 8 April 2022

Accepted: 27 June 2022

Published: 30 June 2022

Publisher's Note: MDPI stays neutral with regard to jurisdictional claims in published maps and institutional affiliations.



Copyright: © 2022 by the authors. Licensee MDPI, Basel, Switzerland. This article is an open access article distributed under the terms and conditions of the Creative Commons Attribution (CC BY) license (<https://creativecommons.org/licenses/by/4.0/>).

1. Introduction

The microphysical processes of clouds and precipitation play vital roles in the formation and development of precipitation and the prediction of severe weather. Raindrop size distribution (DSD) is an important feature that characterizes the microphysical process of precipitation [1–3] and is mainly affected by climatic characteristics and precipitation types [3–9]. In recent years, disdrometer DSD measurements have been widely used to study the microphysical characteristics of precipitation [4,10–14]. Many DSD observations and analyses have been carried out in different regions of China. Based on the OTT Particle Size Velocity (PARSIVEL) disdrometer data from Nagqu (4500 m above sea level (ASL)) over the Tibetan Plateau (TP), Chen et al. [15] reported that the discrepancy in DSDs between day and night is nonsignificant in stratiform rainfall but obvious in convective rainfall. The DSDs of different precipitation types (stratiform and convective) between Nagqu over the TP and Yangjiang in southern China were compared and showed that all three gamma parameters for stratiform precipitation over the TP are larger than those in southern China, while the normalized intercept parameter N_w and the shape parameter

μ for convective precipitation are less than those in southern China [16]. DSD statistical analysis was also conducted in Yining, Xinjiang, an arid region of China, and it showed that convective precipitation was neither continental-like nor maritime-like [17]. In addition, the same location will display significant seasonal differences in the microphysical processes of precipitation [18]. The precipitation over the South China Sea (SCS) is dominated by small (midsize) drops during the premonsoon (monsoon) period, while it has the lowest concentration of raindrops in the postmonsoon season [18]. Monsoon precipitation at Thiruvananthapuram, a coastal tropical station in India, has a higher concentration of small drops than in the other three seasons [3]. Krishna et al. [6] found that the mean concentrations of medium and large raindrops in the west monsoon season are higher than those in the east monsoon season in the Palau Islands.

The TP is located in western China, with an average elevation of approximately 4000 m. It is important to the climate and ecosystems of the Asian continent and even the world [19]. The TP is also known as the Water Tower of Asia due to the origination of seven important Asian rivers, including the Yellow River, the Yangtze River, the Yarlung Zangbo River, etc. The westerlies–monsoon synergy zone covers the TP and the surrounding areas. Climate warming has led to anomalies in westerlies–monsoons and an imbalance in the Water Tower of Asia. The Yarlung Zangbo Grand Canyon (YGC), with a total length of 496.3 km and a depth of up to 6009 m [20], is located in the southeast TP and is the largest channel for transporting water vapor to the TP. During the Indian summer monsoon period, warm and wet water vapor is transported northward to the TP along the YGC. The water vapor transport intensity (nearly $2000 \text{ g cm}^{-1} \text{ s}^{-1}$) is equivalent to that from the south bank of the Yangtze River to the north bank in summer [21]. The YGC plays an important role in climate change in the TP and is a typical unit in the TP climate system.

Médog, with a mean altitude of 1200 m, is located at the entrance of the YGC. The humid air from the Indian Ocean flows straight into the gorge, giving Médog the most annual accumulated precipitation on the TP [22]. Due to inconvenient transportation and frequent debris flows in the rainy season, in situ observation data are lacking along the YGC, especially in Médog. To explore the causes and related mechanisms of water resource changes in the Yarlung Zangbo River basin under the synergistic action of westerlies–monsoons in the southeast TP, a comprehensive cloud precipitation observation test base was established at the Médog Climate Observatory (95.32°E , 29.31°N), supported by “the Second Tibetan Plateau Scientific Expedition” and “the Earth-Atmosphere Interaction in the TP and its Influence on the Weather and Climate in the Lower Reaches” projects. A Ka-band cloud radar, a micro rain radar, an OTT PARSIVEL disdrometer and other instruments were deployed at Médog National Climate Observatory to obtain the three-dimensional structure of clouds and precipitation characteristics in the YGC. Based on Ka-band cloud radar measurements, the vertical structure characteristics and diurnal variation in clouds over Médog in the southeast TP were analyzed [23]. In addition, precipitation in Médog was dominated by small and medium drops, and the convective rain in this region could be classified as maritime-like [24]. However, the seasonal variation characteristics of the raindrop spectrum were not analyzed due to the short observation period. In this study, DSD data collected from an OTT PARSIVEL disdrometer during the period of July 2019 to June 2020 were used to study the seasonal variation in microphysical characteristics for different precipitation intensities and precipitation types. In addition, the European Centre for Medium-Range Weather Forecasts (ECMWF) Reanalysis version 5 (ERA5) data, Fengyun-4A (FY-4A) satellite products and automatic weather station (AWS) observations were used to address the possible reasons for the seasonal differences in DSDs in Médog. This study aimed to better understand the seasonal variation in the microphysical characteristics of precipitation processes at the entrance of the water vapor channel in the YGC and its relationship with westerlies–monsoon synergy and water vapor transport, which is beneficial for improving the microphysical parameterization scheme and the precipitation forecast of the models in the TP.

The instruments, data and methods adopted in this study are provided in Section 2. The properties of DSDs and microphysics parameters for different rain rate classes and precipitation types in different seasons are reported in Section 3. Section 4 discusses the possible reasons for the seasonal variations in DSDs. The major conclusions are given in the final section.

2. Data and Methods

The proposed research investigation used different datasets to provide an overall evaluation of seasonal variation in raindrop size distribution in Mèdog. The main steps followed along this study are presented in the flow chart depicted in Figure 1.

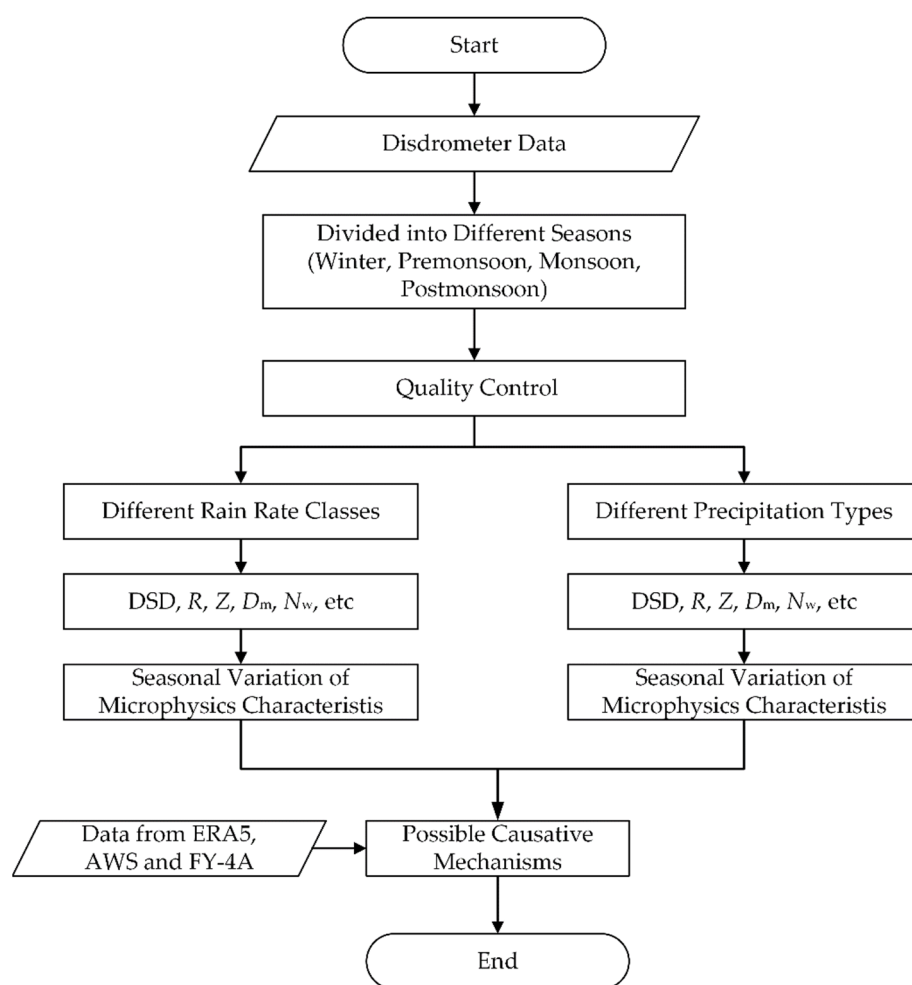


Figure 1. Methodological workflow diagram adopted in this study.

Measurements from a laser-optical PARSIVEL disdrometer [7] in Mèdog with a time resolution of 1 min were used in this study. The position of the Mèdog National Climate Observatory and a picture of the PARSIVEL disdrometer are shown in Figure 2. A disdrometer can simultaneously measure the size and falling speed of hydrometeors. The size and falling speed ranged from 0.06 mm to 24.5 mm and from 0.05 to 20.8 m s⁻¹, respectively, which were divided into 32 nonequidistant bins [25,26].

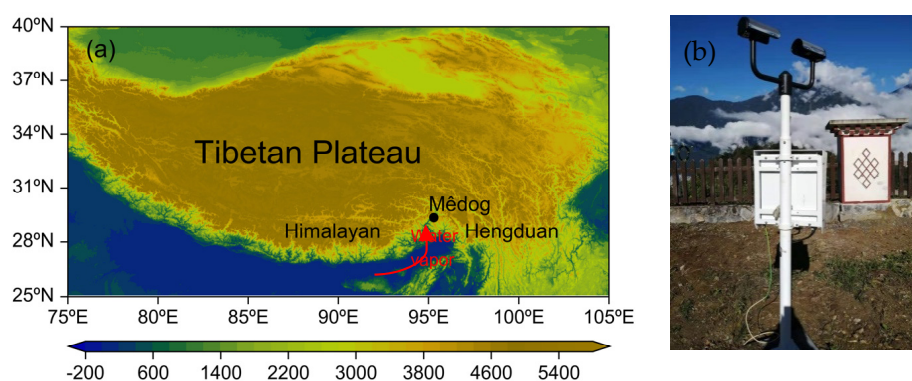


Figure 2. The locations of Médog (black solid dot) and Yarlung Zangbo Grand Canyon (YGC), and topography (m) of the Tibetan Plateau (TP) (a) and the PARSIVEL disdrometer (b). The red arrow indicates water vapor channel in the YGC.

The disdrometer data used in this study were collected from 1 July 2019 to 30 June 2020 and divided into four periods, winter (January–February), premonsoon (March–May), monsoon (June–September) and postmonsoon (October–December) [3], to study the seasonal characteristics of DSDs in Médog. During this period, 30 days and 893 min of data were missing due to power outages caused by geological disasters, such as landslides and debris flows.

2.1. Quality Control

In this study, strict quality control was carried out on disdrometer data to eliminate the influence of raindrop classification errors caused by edge landing, strong wind and splashing. Firstly, the falling speed beyond the boundary of $\pm 60\%$ of Beard's empirical speed–diameter relationship was excluded [27]. Given the terrain altitude of Médog, the speed–diameter relationship was corrected by multiplying by an air density factor of 1.04 [28]. Figure 3 gives the accumulated raw particle counts by diameter and fall speed observed during the four seasons. Drops beyond a $\pm 60\%$ empirical fall speed–diameter relationship were eliminated. The distribution of fall speed–diameter basically conformed to Beard's empirical fall speed–diameter relationship after quality control.

Secondly, the first and second size bins were removed due to their low signal-to-noise ratio, and the size bins with a number of drops less than 2 or with diameters greater than 6 mm were screened and eliminated [10]. One-minute samples with a total number of raindrops less than 10 or a rainfall rate less than 0.1 mm h^{-1} were regarded as instrument noise and eliminated [3,29]. Good agreements between disdrometer observations and gauge measurements in Médog have been reported by Wang et al. [24], although disdrometers tend to underestimate gauged rain. This suggests that disdrometer data could be used to explore the seasonal variation in the microphysical characteristics of precipitation in Médog.

A total of 73,707 min of precipitation samples after quality control were collected from the disdrometer at the Médog National Climate Observatory, with accumulated rainfall of 1237.57 mm. Table 1 shows the total rain duration and accumulated rainfall amount during the four seasons. As seen from Table 1, Médog precipitation mainly occurred in the monsoon period, with the rainfall in this period being 699.92 mm, accounting for approximately 57% of the total, followed by the premonsoon period, accounting for approximately 32%. The rainfall in winter was the lowest, accounting for only approximately 4% of the total rainfall. Rainfall exhibited obvious seasonal variation.

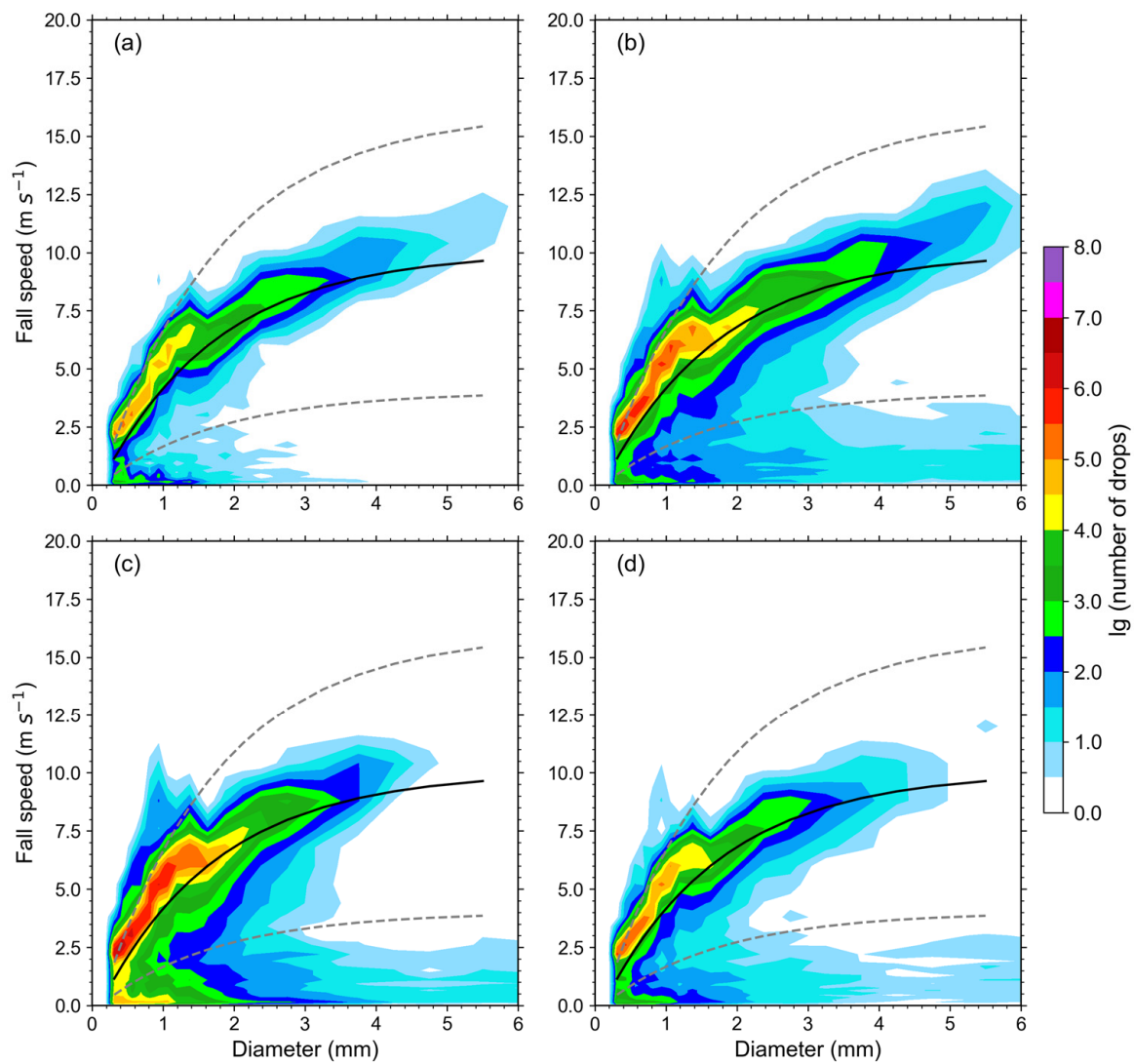


Figure 3. Accumulated raw particle counts by diameter and fall speed were observed during the four seasons: winter (a), premonsoon (b), monsoon (c) and postmonsoon (d). Solid black lines indicate the empirical fall speed–diameter relationship. Dashed lines denote the $\pm 60\%$ empirical fall speed–diameter relationship.

Table 1. Total rain duration and accumulated rainfall amount during the four seasons.

Season	Total Rain Duration (min)/Frequency (%)	Accumulated Rainfall (mm)/Percentage (%)
Winter	6153/8.35	48.90/3.95
Pre-mon	24,880/33.75	400.76/32.38
Monsoon	35,538/48.22	699.92/56.56
Post-mon	7136/9.68	87.99/7.11

2.2. Parameter Calculation

The raindrop number ($n_{i,j}$) of the i th size (D_i) and the j th speed (V_j) are measured by a disdrometer. The raindrop number concentration, $N(D_i)$ ($\text{m}^{-3} \text{mm}^{-1}$), in the i th size can be calculated as follows:

$$N(D_i) = \sum_{j=1}^{32} \frac{n_{i,j}}{V_j \times S/T \times \Delta D_i} \quad (1)$$

where S (m^2) and T (s) are the sampling area and sampling time and were set to 54 cm^2 and 60 s in this study, respectively. ΔD_i indicates the size interval.

The rainfall rate R (mm h^{-1}), radar reflectivity factor Z ($\text{mm}^6 \text{ m}^{-3}$), total raindrop concentration N_T (m^{-3}) and liquid water content (LWC, g m^{-3}) can be obtained from the following equations:

$$R = 6\pi \times 10^{-4} \sum_{i=3}^{32} \sum_{j=1}^{32} D_i^3 \frac{n_{i,j}}{S \times T} \quad (2)$$

$$Z = \sum_{i=3}^{32} D_i^6 N(D_i) \Delta D_i \quad (3)$$

$$N_T = \sum_{i=3}^{32} N(D_i) \Delta D_i, \quad (4)$$

$$\text{LWC} = \frac{\pi}{6000} \sum_{i=3}^{32} D_i^3 N(D_i) \Delta D_i, \quad (5)$$

In this paper, the gamma distribution model was used to fit the observed DSDs from the disdrometer [30]:

$$N(D) = N_0 D^\mu \exp(-\Lambda D) \quad (6)$$

where D (mm) represents the hydrometeor diameter, N_0 ($\text{mm}^{-\mu-1} \text{ m}^{-3}$) is the intercept parameter, and Λ (mm^{-1}) and μ indicate the slope parameter and shape parameter, respectively. Λ and μ can be calculated as follows [31]:

$$M_x = \sum_{i=3}^{32} N(D_i) D_i^x \Delta D_i, \quad (7)$$

$$G = \frac{M_4^3}{M_3^2 M_6}, \quad (8)$$

$$\mu = \frac{11G - 8 + \sqrt{G(G+8)}}{2(1-G)}, \quad (9)$$

$$\Lambda = (\mu + 4) \frac{M_3}{M_4}. \quad (10)$$

Testud et al. [32] proposed the normalized gamma distribution:

$$N(D) = N_w f(\mu) \left(\frac{D}{D_m}\right)^\mu \exp\left[-(4+\mu)\frac{D}{D_m}\right], \quad (11)$$

$$f(\mu) = \frac{\Gamma(4) (4+\mu)^{4+\mu}}{4^4 \Gamma(4+\mu)}, \quad (12)$$

where $\Gamma(x)$ represents a complete gamma function that is defined as follows:

$$\Gamma(x) = \sqrt{2\pi} e^{-x} x^{x-\frac{1}{2}} \quad (13)$$

The mass-weighted mean diameter D_m (mm) and normalized intercept parameter N_w ($\text{m}^{-3} \text{ mm}^{-1}$) can be used to describe the general DSD characteristics and can be defined as follows [33]:

$$D_m = \frac{M_4}{M_3}, \quad (14)$$

$$N_w = \frac{256}{6} \times \frac{M_3^5}{M_4^4}. \quad (15)$$

2.3. Different Classes in R , D_m and N_T

The DSD data used in this study were divided into the following six categories according to R , D_m and N_T , respectively, as shown in Table 2. Percentages of occurrence

and relative contributions to total rainfall were calculated for different categories of R , D_m and N_T . To improve the representativeness of the statistical characteristics, the rainfall rate categories with fewer than 20 samples were excluded.

Table 2. Categories of rain rate (R), mass-weighted mean diameter (D_m) and total raindrop concentration (N_T).

Rain Rate (R)		Mass-Weighted Mean Diameter (D_m)		Total Raindrop Concentration (N_T)	
Variable	Range, mm h ⁻¹	Variable	Range, mm	Variable	Range, m ⁻³
R1	0.1–1	D _m 1	<1	N _T 1	10–250
R2	1–2	D _m 2	1–2	N _T 2	250–500
R3	2–5	D _m 3	2–3	N _T 3	500–750
R4	5–10	D _m 4	3–4	N _T 4	750–1000
R5	10–20	D _m 5	4–5	N _T 5	1000–1500
R6	>20	D _m 6	>5	N _T 6	>1500

2.4. Different Precipitation Types

To further analyze the DSD characteristics in different seasons, the 1 min DSD samples from the disdrometer were also classified into stratiform rainfall and convective rainfall according to a simple method based on the SD σ_R of rainfall rate R [34]. Specifically, for 10 continuous 1 min DSD samples, if $R \geq 5$ mm h⁻¹ and $\sigma_R > 1.5$ mm h⁻¹, convective rainfall was distinguished, while when $\sigma_R \leq 1.5$ mm h⁻¹, stratiform rainfall was classified.

In addition to the disdrometer measurements, ECMWF ERA5 reanalysis data, AWS observations and FY-4A products were also used in this study. ERA5 reanalysis data are the fifth-generation ECMWF reanalysis for the global climate and weather for the past 4 to 7 decades recorded by C3S Climate Data Store (CDS, <https://cds.climate.copernicus.eu>, accessed on 1 September 2021) with a spatial resolution of 0.25° × 0.25°. FY-4A is China's second-generation geostationary meteorological satellite and carries the Advanced Geosynchronous Radiation Imager (AGRI), the Geostationary Interferometric Infrared Sounder (GIIRS) and the Lighting Mapping Imager (LMI). AGRI has 14 channels, and the spatial resolution can reach 0.5–1 km for visible and near-infrared bands and 2–4 km for infrared bands. The AGRI level2 dataset provides the cloud type (CLT), the cloud top height (CTH), the Black Body Temperature (TBB) and other products, which can be obtained at FENGYUN Satellite Data Center (<http://satellite.nsmc.org.cn>, accessed on 1 September 2021).

3. Result

3.1. Statistical Characteristics

Table 3 shows the maximum, mean and standard deviation (SD) of R , D_m and N_T calculated by using 1 min DSD disdrometer samples in different seasons. The maximum rainfall rate of 56.643 mm h⁻¹ was in the premonsoon season, indicating that the strongest convective precipitation occurred in the premonsoon season. The mean R was highest in the monsoon season, followed by the premonsoon season, and the weakest in winter. The sequence was in line with that of the accumulated rainfall amount in the four seasons. The low value of SD in all the seasons indicated a small variation in precipitation intensity in Mèdog. The lowest SD in winter may be related to uniform stratiform precipitation and minimal convective precipitation. The higher SD was more or less in the premonsoon and monsoon seasons, showing that convective precipitation mainly occurred in the two seasons.

Table 3. Maximum, mean and standard deviation of R , D_m and N_T during the four seasons.

		Winter	Pre-Mon	Monsoon	Post-Mon
R (mm h ⁻¹)	Max	7.645	56.650	43.980	24.016
	Mean	0.477	0.966	1.182	0.740
	SD	0.563	1.668	1.733	1.184
D_m (mm)	Max	2.970	3.645	3.168	3.314
	Mean	0.976	1.021	0.900	0.923
	SD	0.258	0.287	0.237	0.236
N_T (m ⁻³)	Max	810.352	1914.562	2401.187	1449.321
	Mean	96.262	156.808	279.416	176.428
	SD	57.739	130.039	217.689	167.339

The maximum, mean and SD of D_m were found to be larger in the premonsoon season, which indicates stronger convective actions. During the monsoon season, the mean and SD of D_m were smaller, probably due to precipitation dominated by warm rain processes and the relative consistency of precipitation [3,24]. The maximum, mean and SD of N_T were the highest in the monsoon season, which indicates that the raindrop concentration was the highest with larger dispersion.

In general, the monsoon exhibited the largest values for the mean and SD of R , the smallest values for the mean and SD of D_m , and the highest values for the maximum, mean and SD of N_T . All these features showed that rainfall during the monsoon period is characterized by abundant, smaller drops, which may be attributed to the sufficient warm and humid air flows from the Indian Ocean. In addition, the D_m of premonsoon precipitation registered larger values in the maximum, mean and SD, as well as the highest value of the maximum R . Therefore, stronger convective activities probably occurred in the premonsoon season.

3.2. Seasonal Variation in DSDs

Figure 4 shows the DSDs of different seasons from mean spectra. Drops with $D \leq 1$ mm were regarded as small raindrops, $D > 3$ mm as large raindrops, and $1 < D \leq 3$ mm as medium raindrops [18]. As seen from Figure 4, the DSDs in Mèdog exhibited bimodal distribution with peaks at 0.4 mm and 1.1 mm. This characteristic of the multippeak raindrop spectrum has been discussed [35]. In terms of small raindrops, the highest concentration was in the monsoon season and the lowest was in winter, and the premonsoon season was similar to the postmonsoon season. As raindrop diameter increased, the concentration of medium raindrops was slightly higher in the monsoon and premonsoon seasons than in the postmonsoon and winter seasons. The concentration of large raindrops was the highest (lowest) in the premonsoon (monsoon) season. The results showing that the concentration of large (small) raindrops was the highest in the premonsoon season (monsoon) were consistent with those found in tropical coastal areas, which are also dominated by the Indian Ocean monsoon in summer [3]. Unlike the SCS, Zeng et al. [18] reported that small drops predominate in precipitation during the premonsoon period, while large drops prevail in the postmonsoon season.

To further analyze the DSD characteristics in different seasons, the DSD data used in this study were divided into six categories, as shown in Table 2. The DSDs of different rainfall rate categories from mean spectra for different seasons are shown in Figure 5. As the rainfall rate increased, the spectra width in all seasons became wider, and the difference in DSDs among the four seasons gradually increased. For $R < 5$ mm h⁻¹ (usually corresponding to stratiform precipitation [13]), the concentration of large raindrops was the highest in winter. Precipitation with $R \geq 10$ mm h⁻¹ (usually corresponding to convective rainfall [36,37]) occurred mainly in the premonsoon and monsoon seasons. The concentration of large raindrops in the premonsoon season was significantly greater than that in the monsoon season, indicating stronger convective rainfall in the premonsoon season.

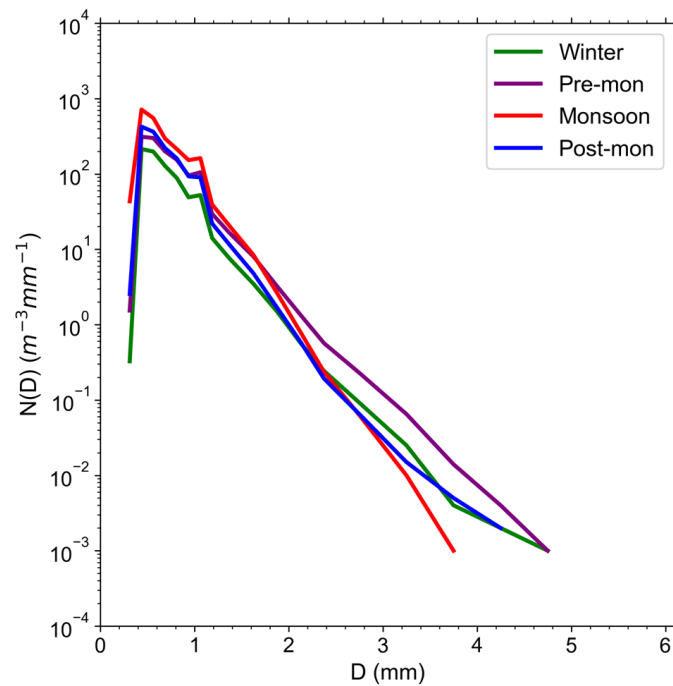


Figure 4. Averaged DSDs during the four seasons.

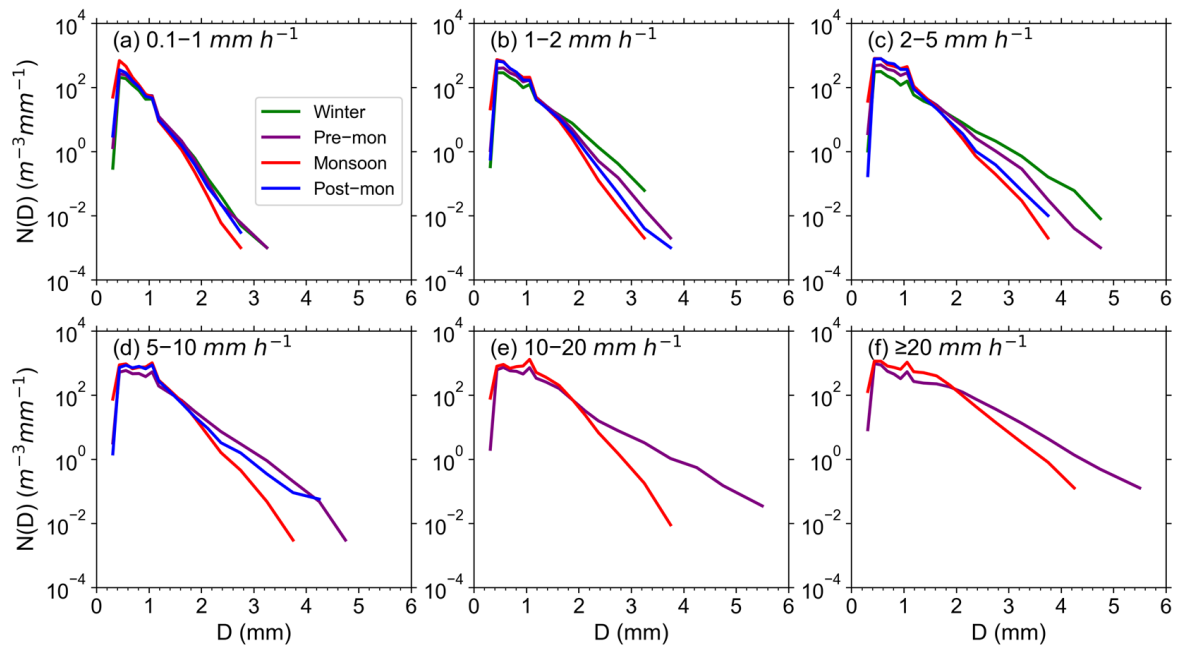


Figure 5. Averaged DSDs for different rain rate categories. (a) R1: $0.1 \leq R < 1 \text{ mm h}^{-1}$, (b) R2: $1 \leq R < 2 \text{ mm h}^{-1}$, (c) R3: $2 \leq R < 5 \text{ mm h}^{-1}$, (d) R4: $5 \leq R < 10 \text{ mm h}^{-1}$, (e) R5: $10 \leq R < 20 \text{ mm h}^{-1}$ and (f) R6: $R \geq 20 \text{ mm h}^{-1}$.

Table 4 gives the average rainfall microphysical parameters for each of the six rainfall rate categories from 1 min DSD samples in different seasons. The mean values of Z , LWC, N_T and D_m increased with increasing rain rate in all seasons. The $\log_{10}(N_w)$ tended to decrease with the increasing rain rate in winter, indicating that the increase in precipitation intensity was mainly attributed to the increase in raindrop size. During other periods, $\log_{10}(N_w)$ tended to increase with increasing rain rate until $R > 20 \text{ mm h}^{-1}$. For the same rainfall rate categories, monsoon precipitation was characterized by the smallest mean D_m value and the highest mean $\log_{10}(N_w)$ value.

Table 4. Average rainfall microphysical parameters for each of the six rainfall rate classes in the winter, premonsoon, monsoon and postmonsoon seasons.

	Class (mm h ⁻¹)	Samples	R (mm h ⁻¹)	Z (dBZ)	LWC (g m ⁻³)	N _T (m ⁻³)	D _m (mm)	log ₁₀ (N _w) (N _w in m ⁻³ mm ⁻¹)	μ
Winter	0.1 ≤ R < 1	5546	0.332	17.110	0.019	87.880	0.923	3.297	10.037
	1 ≤ R < 2	444	1.368	27.000	0.066	161.317	1.356	3.222	4.415
	2 ≤ R < 5	152	2.752	33.175	0.118	192.405	1.729	3.063	2.960
	5 ≤ R < 10	11	-	-	-	-	-	-	-
	10 ≤ R < 20	-	-	-	-	-	-	-	-
	R ≥ 20	-	-	-	-	-	-	-	-
Pre-mon	0.1 ≤ R < 1	17,796	0.406	17.511	0.024	112.441	0.919	3.395	11.940
	1 ≤ R < 2	4304	1.401	25.261	0.072	221.116	1.171	3.517	7.066
	2 ≤ R < 5	2338	2.905	30.741	0.138	311.241	1.394	3.508	5.732
	5 ≤ R < 10	352	6.420	35.292	0.287	456.934	1.574	3.626	6.271
	10 ≤ R < 20	63	13.795	40.876	0.574	639.370	1.864	3.667	6.528
	R ≥ 20	27	32.590	46.225	1.211	736.530	2.336	3.525	5.495
Monsoon	0.1 ≤ R < 1	22,605	0.423	16.254	0.028	205.271	0.797	3.729	14.108
	1 ≤ R < 2	7248	1.418	23.496	0.079	324.584	1.021	3.787	8.802
	2 ≤ R < 5	4710	2.954	27.882	0.153	463.498	1.134	3.889	2.853
	5 ≤ R < 10	782	6.636	31.735	0.327	732.233	1.205	4.114	10.112
	10 ≤ R < 20	154	13.132	36.175	0.609	900.956	1.381	4.141	9.568
	R ≥ 20	39	26.385	42.061	1.130	1095.38	1.743	4.004	6.803
Post-mon	0.1 ≤ R < 1	5678	0.370	16.568	0.023	127.712	0.874	3.462	13.122
	1 ≤ R < 2	968	1.378	24.120	0.076	303.602	1.069	3.701	8.052
	2 ≤ R < 5	412	2.844	28.385	0.147	456.403	1.165	3.848	8.263
	5 ≤ R < 10	62	6.664	33.567	0.320	670.792	1.330	3.981	8.917
	10 ≤ R < 20	13	-	-	-	-	-	-	-
	R ≥ 20	3	-	-	-	-	-	-	-

3.3. Distribution of D_m, R, and N_T

Figure 6 shows the percentage of occurrence (bar) and relative contribution to the total rainfall (line) for the different D_m bins in the four seasons. Médog rainfall in all the seasons was dominated by raindrops with D_m < 2 mm. The distribution of the occurrence frequency of D_m was similar in all seasons except for a slight difference in the premonsoon season. The occurrence frequency of D_{m1} was the highest, followed by D_{m2} for all four seasons. During the winter, monsoon and postmonsoon seasons, the occurrence percentage of D_{m1} was more than 60%, whereas it was less than 60% during the premonsoon period. On the other hand, the percentage occurrence of D_{m2} was more than 40% in the premonsoon season, while it was approximately 30% in the other three seasons. The decreased D_{m1} in the premonsoon season was compensated by the increase in D_{m2}. This result indicated that the occurrence frequency of larger raindrops was higher in the premonsoon season than in the other three seasons.

The distribution of the relative contribution to the rainfall totals was different from that of the occurrence frequency. The D_{m2} category produced a greater contribution to rainfall by 50–70%, although it had a lower occurrence frequency than the D_{m1} category. The rainfall rate was proportional to the third power of raindrop diameter. The larger raindrops with 2 ≤ D_m < 3 mm only contributed to the total rainfall by approximately 5% in the winter and premonsoon seasons, and there were hardly any larger raindrops with 2 ≤ D_m < 3 mm during the monsoon and postmonsoon periods.

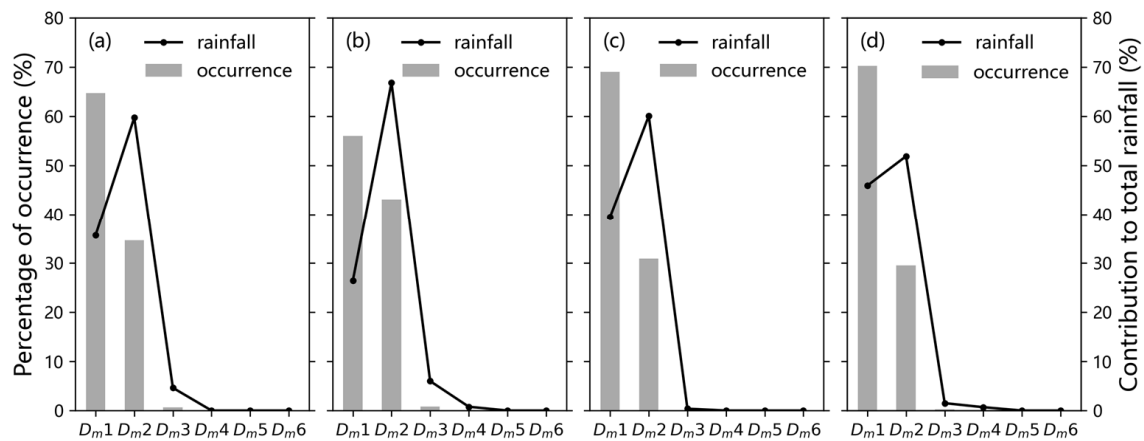


Figure 6. Percentages of occurrence (bar) and relative contributions to the total rainfall (line) from the different D_m bins in the four seasons: winter (a), premonsoon (b), monsoon (c) and postmonsoon (d).

The percentage of occurrence (bar) and relative contribution to the total rainfall (line) from the different rain rate categories in the four seasons are shown in Figure 7. Weak rainfall with $R < 1 \text{ mm h}^{-1}$ was dominant in the four seasons, which was evident from the occurrence frequency of the R1 category exceeding 60%, especially more than 80% in the winter season. The occurrence frequencies of R2 and R3 were higher in the monsoon season than in the other three seasons. Considering the relative contribution to total rainfall, the relative contribution to rainfall by R1 was largest and exceeded 60% in the winter season. Similarly, the R1 category also made the largest relative contribution to rainfall in the postmonsoon season. However, the relative contributions to rainfall by the R1, R2, and R3 categories were comparable in the premonsoon season. During the monsoon season, the R3 category made the highest contribution to total rainfall, although its occurrence frequency was lower than that of the R1 and R2 categories.

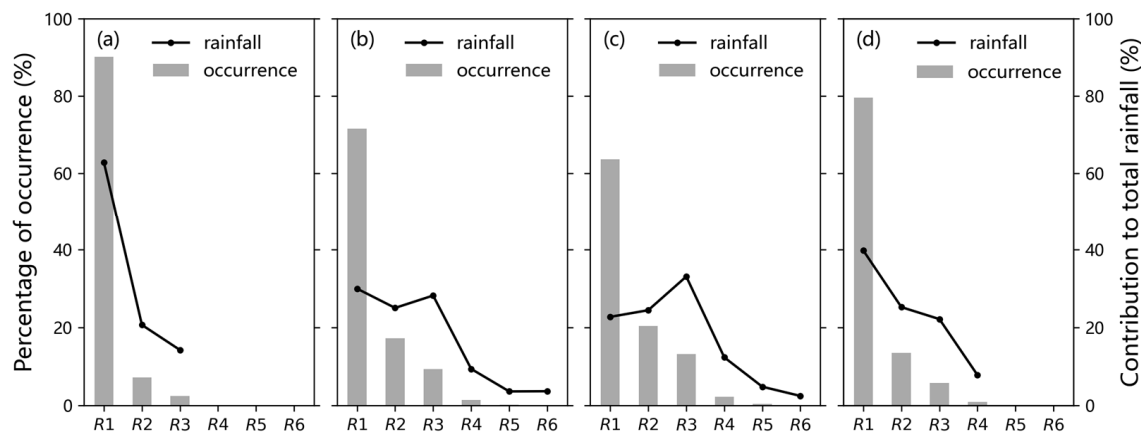


Figure 7. Percentages of occurrence (bar) and relative contributions to the total rainfall (line) from the different R bins in the four seasons: winter (a), premonsoon (b), monsoon (c) and postmonsoon (d).

Figure 8 shows the percentage of occurrence (bar) and relative contribution to the total rainfall (line) from the different N_T classes in the four seasons. The occurrence frequencies decreased with the increase in drop number, and the N_T1 class predominated in the four seasons. The drop concentration in Médog was mostly below 250 m^{-3} , followed by $250\text{--}500 \text{ m}^{-3}$, and a drop concentration of more than 1000 m^{-3} rarely occurred. The occurrence frequency of N_T1 was lower in the monsoon season (approximately 57%) than in the other three seasons (an average of approximately 88%), and the occurrence frequency of N_T2 in the monsoon season (approximately 30%) was higher than in the other three seasons (an average of approximately 9.5%). The relative contribution to the total rainfall

monotonically decreased with increasing N_T in all seasons except the monsoon season. During the monsoon season, N_{T2} made a larger relative contribution (38%) to the total rainfall than the N_{T1} class (28%).

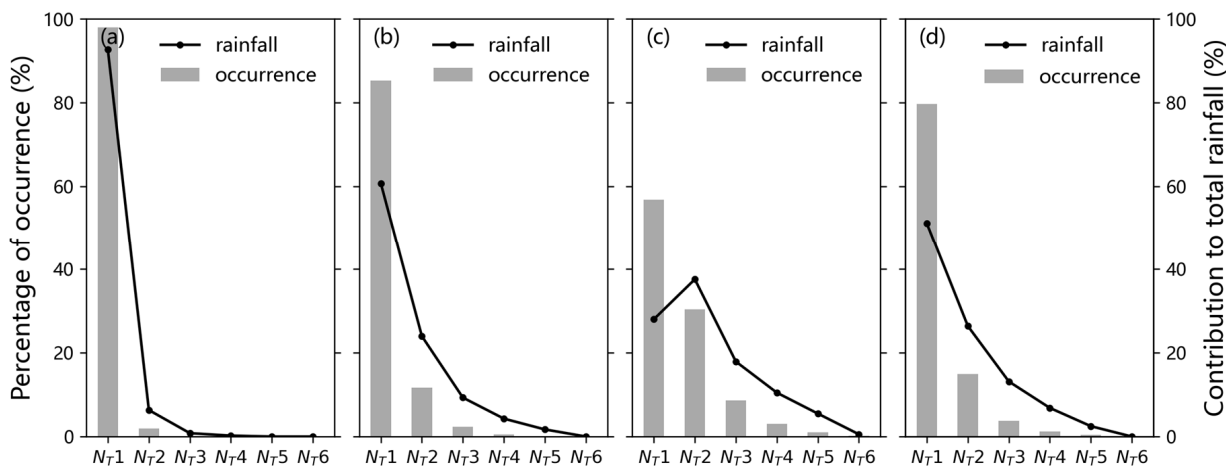


Figure 8. Percentages of occurrence (bar) and relative contributions to the total rainfall (line) from the different N_T bins in the four seasons: winter (a), premonsoon (b), monsoon (c) and postmonsoon (d).

3.4. Characteristics of DSDs in Stratiform and Convective Rainfall

Previous studies have shown that the microphysical process of stratiform rainfall is significantly different from that of convective rainfall [34,38]. Therefore, the 1 min DSD samples were classified into stratiform rainfall and convective rainfall. Consequently, the stratiform/convective precipitation samples/percentages were 6130/5 (99.6%/0.1%), 24,155/286 (97.1%/1.1%), 33,468/763 (94.2%/2.1%) and 6930/69 (97.1%/1.0%) in the winter, premonsoon, monsoon and postmonsoon seasons, respectively. Considering only five samples, the DSD of convective rainfall in winter was not considered.

Figure 9 shows the DSDs of stratiform rainfall and convective rainfall from mean spectra during different periods. Compared to stratiform rainfall, convective rainfall had a broader spectrum width and a higher concentration of drops. Bimodal distribution could also be seen in both DSDs of stratiform rain and convective rain, and the concentration of the second peak at 1.1 mm was comparable to that of the first peak at 0.4 mm for convective rainfall.

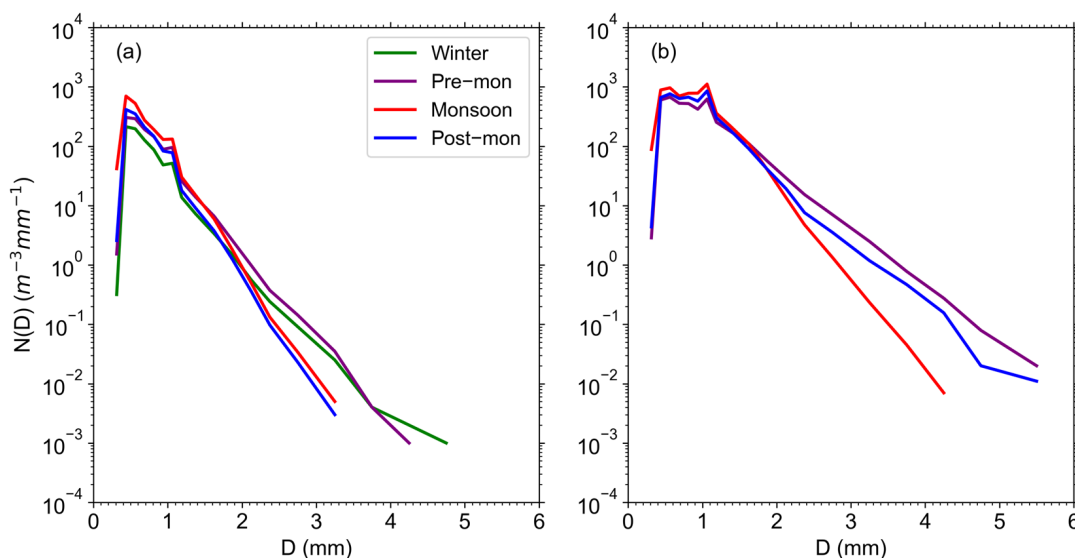


Figure 9. The mean DSDs of stratiform rain (a) and convective rain (b) for different seasons.

For stratiform rainfall (Figure 9a), the DSD peaked at 0.4 mm in all four seasons and then decreased rapidly. The precipitation in the monsoon season (winter) was characterized by a higher (lower) concentration of drops with sizes less than 1.1 mm. The winter and premonsoon precipitation had higher concentrations of drops with sizes larger than 2.1 mm than the monsoon and postmonsoon precipitation. The precipitation in the four seasons had comparable concentrations of drops with diameters of 1.1–2.1 mm. For convective rainfall (Figure 9b), the highest concentration of raindrop diameters less than 1.1 mm occurred in the monsoon season, and the highest concentration of drops larger than 1.7 mm appeared in the premonsoon season. On the other hand, convective rain in the monsoon season had the lowest concentration of larger drops with $D > 2$ mm, and the lowest concentration of small drops occurred in the premonsoon season. The concentrations of raindrops with sizes of 1.1–1.7 mm were very similar for the three seasons considered.

The average microphysical parameters of stratiform rain and convective rain from 1 min DSD samples during the four periods are given in Table 5. For stratiform rain, the mean LWC, N_T , R , N_w and μ were the highest in the monsoon season. The largest mean D_m value was observed in the premonsoon season, followed by the winter season, and the smallest mean D_m value was observed in the monsoon season. The highest mean Z in the premonsoon season was mainly attributed to the largest D_m because the reflectivity factor is proportional to the sixth power of drop diameter. During the winter period, the lowest mean R and LWC were probably related to the lowest concentration of drops. For convective rain, the mean R , Z , LWC and D_m were the largest in the premonsoon period. The highest mean values of N_T , N_w and μ were found in the monsoon period, followed by the postmonsoon period, and the lowest mean values of N_T and N_w were found in the premonsoon period.

Table 5. The average microphysical parameters of stratiform rain and convective rain in different seasons.

Rain Types	Samples	R (mm h ⁻¹)	Z (dBZ)	LWC (g m ⁻³)	N_T (m ⁻³)	D_m (mm)	$\log_{10}(N_w)$ (N_w in m ⁻³ mm ⁻¹)	μ
Winter_Str	6130	0.47	21.50	0.02	95.43	0.97	3.28	9.45
Pre-mon_Str	24,155	0.82	23.50	0.04	149.03	1.01	3.42	10.46
Monsoon_Str	33,468	0.95	21.99	0.05	258.47	0.89	3.75	12.24
Post-mon_Str	6930	0.62	20.08	0.04	166.54	0.91	3.51	12.17
Winter_Con	5	-	-	-	-	-	-	-
Pre-mon_Con	286	10.86	39.50	0.45	554.82	1.67	3.70	7.07
Monsoon_Con	763	9.11	34.44	0.43	805.81	1.26	4.14	10.14
Post-mon_Con	69	9.02	37.24	0.41	646.12	1.49	3.88	8.44

Figure 10 shows the average $\log_{10}(N_w)$ versus average D_m value (along with $\pm\sigma$ SD bars) for stratiform rain and convective rain during different periods. The two outlined squares represent the maritime-like and continental-like convective events reported by Bringi et al. [34]. In general, the average D_m versus average $\log_{10}(N_w)$ showed evident seasonal differences in Médog. In terms of convective rain, monsoon precipitation had the smallest (highest) mean D_m ($\log_{10}(N_w)$) value of 1.26 mm (4.14), while premonsoon precipitation was characterized by the largest (lowest) mean D_m ($\log_{10}(N_w)$) value of 1.67 mm (3.70). Convective rain in the monsoon and postmonsoon seasons was similar to maritime-like events, exhibiting smaller D_m and higher $\log_{10}(N_w)$. The convective precipitation during the monsoon and postmonsoon seasons also conformed to the C–S separation line from Thompson et al. [5] for the tropics. Convective events during the premonsoon period were considered to be between maritime- and continental-like events. For stratiform rain, the average D_m versus $\log_{10}(N_w)$ values appeared on the left side (underside) of the C–S separation line, as reported by Bringi et al. [34] (Thompson et al. [5]). The differences in the mean D_m values among the four seasons were relatively slight, whereas the mean $\log_{10}(N_w)$ displayed an evident discrepancy. For example, the mean

$\log_{10}(N_w)$ value of 3.75 in the monsoon season was much higher than that in the winter period, with a value of 3.28.

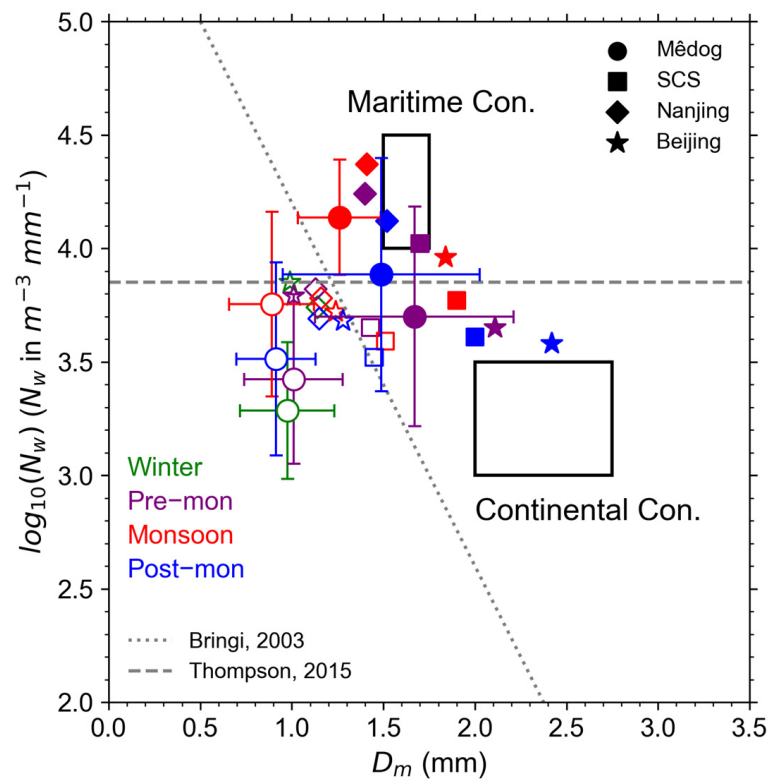


Figure 10. Scatterplots of averaged $\log_{10}(N_w)$ versus D_m (along with $\pm\sigma$ standard deviation bars) for stratiform (blank symbols) and convective (full symbols) precipitation in Médoc (circles), SCS (squares), Nanjing (diamond) and Beijing (star) during the winter (green), premonsoon (purple), monsoon (red) and postmonsoon (blue) seasons. The two outlined squares represent (left) the maritime and (right) continental types of convective systems reported by Bringi et al. [34]. The dotted line and dashed lines represent the C–S separation line by Bringi et al. [34] and Thompson et al. [5].

For comparison with other regions in China, Figure 10 is also superimposed with the mean D_m and $\log_{10}(N_w)$ values of different seasons from previous studies, including the SCS [18], Nanjing [39] and Beijing [40]. Compared with these regions, the stratiform precipitation in Médoc showed smaller mean D_m and mean $\log_{10}(N_w)$ values in all seasons, except the monsoon season, which had a similar mean $\log_{10}(N_w)$ value. The mean D_m value of the premonsoon convective precipitation in Médoc was similar to that in the SCS, and the mean $\log_{10}(N_w)$ value was similar to that in Beijing. Médoc convective rain in the monsoon season was similar to Nanjing, which may have been due to abundant water vapor in the two regions during this period. The mean D_m ($\log_{10}(N_w)$) of Médoc convective rain was much smaller (higher) than that in the SCS and Beijing in the monsoon season. This finding was probably related to the predominant warm (cold) rain processes in Médoc (SCS and Beijing). Similarly, the postmonsoon convective cluster in Médoc was similar to Nanjing but had a smaller (higher) D_m ($\log_{10}(N_w)$) than Beijing and the SCS.

3.5. The μ – Λ Relationships

The μ – Λ relationship is closely related to the DSD and varies with rain types, climatic characteristics and terrain [38,41]. Zhang et al. [38] proposed the quadratic fitting formula in Florida as follows:

$$\Lambda = 0.0365 \mu^2 + 0.735 \mu + 1.935 \quad (16)$$

To minimize the scatter, the samples in Médoc with rain rates $> 5 \text{ mm h}^{-1}$ and drop counts > 300 were used to derive μ and Λ [15,38]. Figure 11 shows the scatterplots of μ

and Λ for three seasons due to minimal convective precipitation in winter. The fitted μ - Λ relationships for the premonsoon, monsoon and postmonsoon periods are given as follows:

$$\Lambda = 0.0148 \mu^2 + 0.786 \mu + 1.916 \quad (17)$$

$$\Lambda = 0.0056 \mu^2 + 0.949 \mu + 1.716, \quad (18)$$

and

$$\Lambda = 0.0250 \mu^2 + 0.665 \mu + 2.674. \quad (19)$$

The μ - Λ relationships in Mèdog exhibited little variation among the different periods, especially for $\Lambda < 13$. The shape factor μ in the postmonsoon season gradually became lower than that in other seasons when $\Lambda > 13$, which may be related to the few samples of convective precipitation with increasing Λ during the postmonsoon period. Notably, the μ - Λ relationships in different seasons were similar to the Florida (subtropical environment) relationship reported by Zhang et al. [38]. This finding might indicate that climatic characteristics may play an important role in the determination of the μ - Λ relationship.

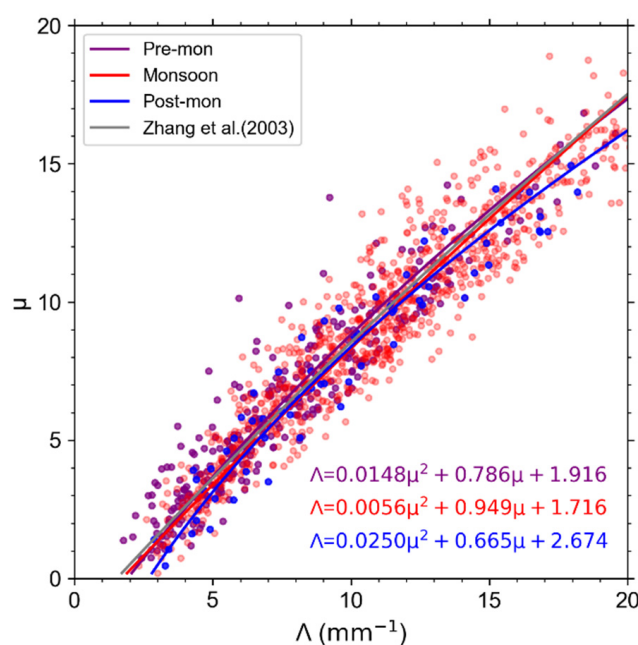


Figure 11. Scatterplots of μ versus Λ and the empirical fitting relationships for samples with rain rates $> 5 \text{ mm h}^{-1}$ and drop counts > 300 during the premonsoon, monsoon and postmonsoon seasons. The colored solid lines are the fitted empirical μ - Λ relationships in different seasons, and the gray solid line represents the empirical μ - Λ relationship of Zhang et al. [38].

3.6. Quantitative Precipitation Estimation (QPE)

An important application of DSD is quantitative precipitation estimation (QPE). The power-law relationship of $Z = AR^b$ is widely used in radar meteorology and changes with rainfall type, atmospheric conditions and geographic location [42]. The new-generation weather radar system in China uses the empirical relationships of $Z = 300R^{1.4}$ and $Z = 200R^{1.6}$ to describe midlatitude convection [43] and stratiform precipitation [44], respectively. Wu and Liu [16] proposed that coefficient A (exponent b) is 170.7 (1.31) and 69.83 (1.83) for summer convection precipitation and stratiform precipitation in Nagqu, respectively, based on disdrometer measurements. Wang et al. [24] gave the relationships of $Z = 114.79R^{1.34}$ and $Z = 53.69R^{1.71}$ for convection precipitation and stratiform precipitation in rainy seasons in Mèdog, respectively. The equivalent radar reflectivity factor (Z_e , in $\text{mm}^6 \text{ m}^{-3}$) based on observed DSDs can be expressed according to Zhang et al. [45]:

$$Z_e = \frac{4\lambda^4}{\pi^4 |K_w|^2} \int_{D_{min}}^{D_{max}} |f(D)|^2 N(D) dD \tag{20}$$

where λ indicates the radar wavelength and was set to 5 cm, considering that C-band Doppler weather radars were deployed over the TP. K_w is the water dielectric factor, and $|K_w|^2$ is set to 0.93 by convention. $f(D)$ is the backscattering amplitude for a raindrop of size D , which is calculated by using the extended boundary condition method (EBCM) [46].

Considering the evident seasonal variation in DSD characteristics in Mèdog, the Z – R relationships for the four seasons are discussed in this section. Figure 12 shows the scatter plots of Z and R superimposed with the fitted Z – R relationships using the least squares method for stratiform rain and convective rain, respectively. The fitted coefficient A and exponent b for different rainfall types in the four seasons are given in Table 6. Following Zeng et al. [18], the normalized mean biases (NBs) of the fitted Z – R relations and empirical relations at midlatitudes for different precipitation types were calculated to evaluate the accuracies of different Z – R relationships (Table 7).

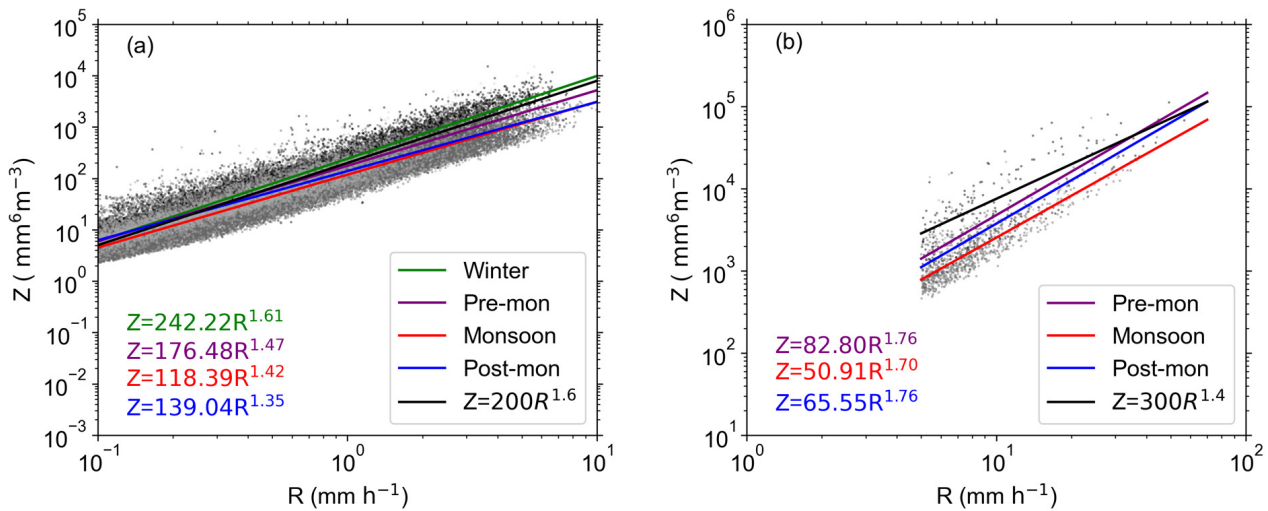


Figure 12. Scatterplots of radar reflectivity factor (Z) and rain rate (R) and fitted Z – R relationships using the least squares method (solid lines) for stratiform rain (a) and convective rain (b).

Table 6. Fitted radar reflectivity and rain rate (Z – R) relationships for stratiform and convective rain types in the four seasons.

Season	Stratiform Rainfall		Convective Rainfall	
	A	b	A	b
Winter	242.22	1.61	-	-
Pre-mon	176.48	1.47	82.80	1.76
Monsoon	118.39	1.42	50.91	1.70
Post-mon	139.04	1.35	65.55	1.76

Table 7. NB (%) values of the fitted Z – R relationships and empirical relationships for different precipitation types in the four seasons.

Season	Stratiform Rainfall		Convective Rainfall	
	Fitted Z – R	$Z = 200R^{1.6}$	Fitted Z – R	$Z = 300R^{1.4}$
Winter	7.91	21.51	-	-
Pre-mon	9.97	−1.74	7.26	−12.27
Monsoon	6.14	−27.24	2.98	−51.38
Post-mon	7.92	−14.32	11.19	−26.87

For stratiform precipitation, a small discrepancy in fitted Z – R relationships among the different seasons could be noted. Winter precipitation had larger A and b values than those of the empirical relationship in midlatitudes, while precipitation in other seasons had smaller A and b values. This result may be related to the fact that winter stratiform precipitation had more (less) large (small) drops than in other seasons. The empirical relationship of $Z = 200R^{1.6}$ underestimated rainfall in the premonsoon, monsoon and postmonsoon seasons by 1.74%, 27.24%, and 14.32%, respectively, while it overestimated winter rainfall by 21.51%. The fitted Z – R relationships reduced the NB to less than 10% for all of the considered seasons.

For convective precipitation, the fitted coefficient A (exponent b) in the premonsoon, monsoon and postmonsoon seasons was much less (larger) than that of the empirical relation at midlatitudes. Monsoon precipitation had a minimum coefficient A (50.91) and exponent b (1.70), which might have been attributed to the large number of small raindrops during this period. That is, the same reflectivity factor would derive the highest rain rate in the monsoon season. Given a radar reflectivity factor value of 40 dBZ, the corresponding rainfall rates were 15.24 mm h^{−1}, 22.33 mm h^{−1} and 18.20 mm h^{−1} in the premonsoon, monsoon and postmonsoon seasons, respectively. The empirical relationship of $Z = 300R^{1.4}$ underestimated convective rainfall up to 51.38% in the monsoon season, followed by 26.87% in the postmonsoon season and then 12.27% in the premonsoon season. However, the fitted Z – R relationships significantly reduced the NB in all of the considered seasons. In particular, the NB decreased from 51.38% to 2.98% in the monsoon season. The distinct seasonal variation in DSDs in Mèdog convective rain determined the evident discrepancy in Z – R relationships among the different seasons. Therefore, the fitted Z – R relationships for different seasons could significantly improve the accuracy of radar-based QPEs.

4. Discussion

The significant seasonal variations in DSDs in Mèdog could provide a better understanding of the microphysical process of precipitation at the entrance of the vapor channel in the YGC and improve the parameterization schemes in numerical models over the TP. The possible causative mechanisms of the distinct DSD variability over seasons may be addressed from the standpoint of the meteorological environments of rainfall [13]. To explore the possible causes of seasonal variations in the DSD in Mèdog, meteorological conditions of rainy days from ERA5 reanalysis data, AWS and TBB and CTH products of the FY-4A satellite were collected. The lifting condensation level (LCL), 0 °C isotherm layer height, CTH, TBB probability density function, surface wind speed box diagram and the vertical integral of water vapor flux of rainy days in the four seasons are shown in Figures 13 and 14.

Due to the lack of radiosonde and ceilometer observations in Mèdog, the LCLs calculated from AWS data were approximately considered as cloud base height (CBH). The average LCL was calculated using the surface temperature (T), surface dew point temperature (T_d) and surface pressure (p) according to the empirical formula (Equations (21)–(23)) given by Barnes [47]:

$$T_{LCL} = T_d - (0.001296T_d + 0.1963)(T - T_d), \quad (21)$$

$$p_{LCL} = p[(T_{LCL} + 273.15)/(T + 273.15)]^{\frac{7}{5}}, \quad (22)$$

$$LCL = 18,400(1 + at) \log\left(\frac{p}{p_{LCL}}\right), \quad (23)$$

T_{LCL} and p_{LCL} indicate the temperature and pressure at LCL height, respectively. $a = 1/273$, $t = T_{LCL} - T$ (unit: °C). The calculated average LCL heights were 0.12 km, 0.13 km, 0.16 km and 0.20 km in the winter, premonsoon, monsoon and postmonsoon periods, respectively, exhibiting a negligible difference in the four seasons. The average heights of the 0 °C isotherm layer from ERA5 in the winter, premonsoon, monsoon and postmonsoon

periods were 1.53 km, 2.67 km, 4.01 km and 2.81 km, respectively, and the average CTHs were 5.13 km, 6.64 km, 6.97 km and 5.39 km, respectively.

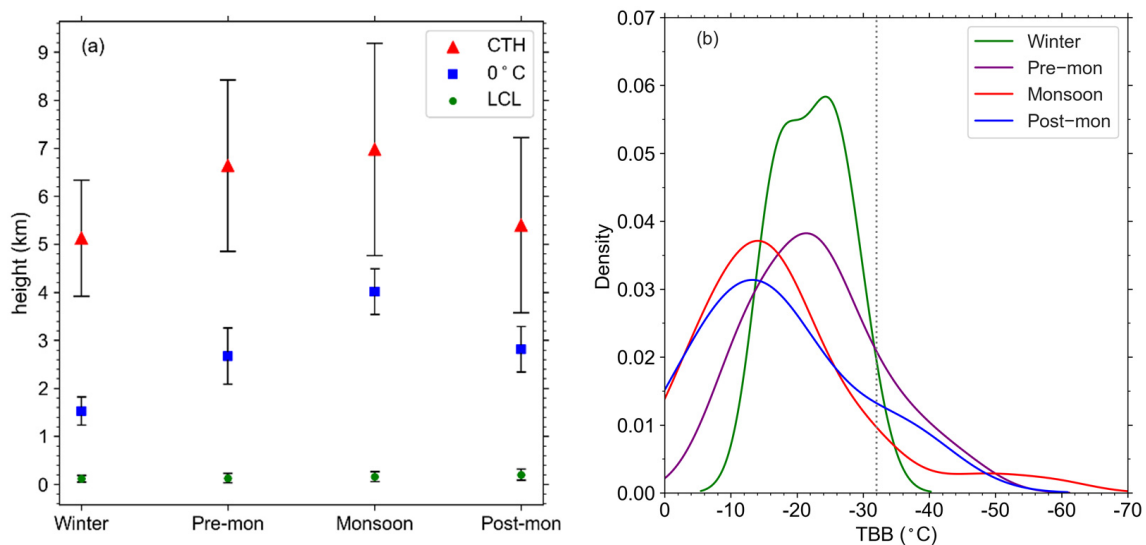


Figure 13. The lifting condensation level (LCL), 0 °C isotherm layer height, cloud top height (CTH) and standard deviation (a). TBB probability density function (b). The dashed line in Figure 13b denotes the TBB temperature of -32 °C.

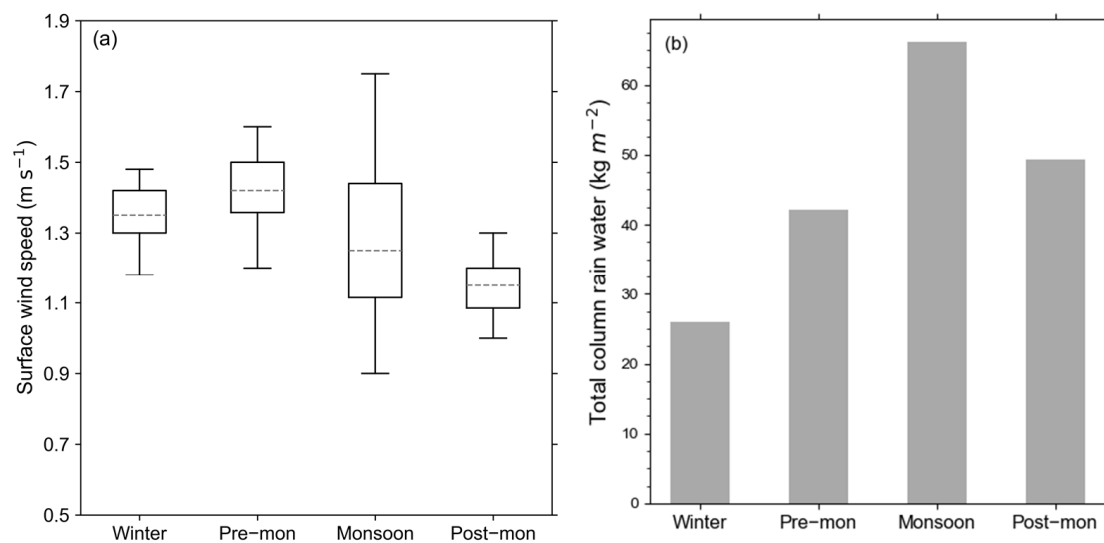


Figure 14. Surface wind speed box diagram (a) and the vertical integral of water vapor flux (b) in different seasons.

Clouds between LCL and the 0 °C isotherm layer level are defined as warm clouds, and those between the 0 °C isotherm layer level and CTH are considered cold clouds [18]. The cloud rain process is predominant during the winter precipitation period, which is evident from the significant cold cloud depth of 3.60 km compared to the relatively short warm cloud depth of 1.41 km. The microphysical and dynamic mechanisms (e.g., updraft, particle formation and particle growth processes) in the cold rain process are different from those in the warm rain process, leading to significant discrepancies in DSD characteristics [39]. Ice crystals grow quickly above the 0 °C isotherm level in the winter precipitation process. The higher concentration of large drops found in winter precipitation may be attributed to melted ice particles, such as low-density, large snow particles, and/or graupel (e.g., Figures 5 and 9a). In addition, wind and humidity are two important meteorological

elements affecting the evaporation process [48]. Stronger evaporation is expected in the winter season due to a larger wind speed and less water vapor (Figure 14), reducing the concentration of small raindrops (e.g., Figures 5 and 9a).

The premonsoon precipitation was characterized by a high concentration of large drops (e.g., Figures 4, 5 and 9). The average cold cloud depth (3.97 km) was much larger than the average warm cloud depth (2.54 km) in the premonsoon season, indicating that the cold rain process is also predominant in this period. The melted ice particles (e.g., graupel and/or snow particles) could result in the formation of larger drops [49]. Convective activity frequently occurs in the premonsoon season, as evidenced by the probability density function (PDF) of TBB (Figure 13b), which is often used to assess the intensity of convective activity [50]. The smaller the TBB value is, the deeper the development of convective clouds. The threshold of $TBB \leq -32$ °C is often used to differentiate the development of convection. The probability of $TBB \leq -32$ °C was the highest in the premonsoon season, indicating that intense convective activity occurs more frequently during this period. The westerly winds prevail over the TP during this period, and cold air masses can easily invade the middle to upper troposphere. In addition, solar radiation causes an increase in surface heating in the daytime. This destabilization of the troposphere would be beneficial to the formation of dry convection in the premonsoon season [51].

In addition, the largest surface wind speed (e.g., Figure 14a) among the four seasons may lead to relatively strong evaporation in the premonsoon season, which was partly responsible for the relatively low concentration of small drops. Thus, a higher concentration of larger raindrops and a lower concentration of small raindrops were observed for higher rainfall rate categories (e.g., $R > 5$ mm h⁻¹) and convective rainfall types (e.g., Figures 5d–f and 9b). Therefore, the intensity increase in premonsoon precipitation was more attributed to the increase in drop diameter (e.g., Table 4).

During the monsoon season, although the CTH was highest, the average thickness of warm clouds (3.85 km) was significantly larger than that of cold clouds (2.96 km) (Figure 13a). Therefore, monsoon rainfall was dominated by warm rain processes, which tended to produce higher concentrations of small raindrops owing to collisional and coalescence processes (e.g., Figures 4, 5 and 9). A large amount of water vapor is carried to Mèdog by the Indian Ocean monsoon in this season (Figure 14b), which is conducive to the formation of warm clouds and the production of abundant small raindrops. Weak evaporation is expected in the monsoon season due to the smaller wind speed and wet environment, contributing to the production of small raindrops. The increase in precipitation intensity in the monsoon season may be mainly attributed to the significant increase in the concentration of raindrops (Table 4).

The postmonsoon precipitation had less rainfall total and was also characterized by a higher concentration of small drops (i.e., Figures 4 and 5b–d). Although the mean depth of warm clouds (2.61 km) was similar to that of cold clouds (2.58 km) in this season, Figure 14 exhibits humid and weak wind atmospheric conditions, which are favorable to the production of small drops.

5. Conclusions

In this paper, the seasonal variation in DSDs and microphysical parameters among the winter, premonsoon, monsoon, and postmonsoon periods were investigated using PARSIVEL disdrometer data from July 2019 to June 2020 in Mèdog, which is located in the southeast of the TP and at the entrance of the vapor channel in the YGC. In addition, EAR5 reanalysis data, FY-4A satellite products and AWS observations were used to address the possible causative factors for the distinct seasonal variation in DSDs. The conclusions of this study are outlined as follows:

(1) Precipitation mainly occurs during the monsoon period in Mèdog, contributing approximately 57% to the annual rainfall totals, and small drops are dominant in the four seasons. Weak rainfall (i.e., $R < 1$ mm h⁻¹) with small drops (i.e., $D_m < 1$ mm) and low concentrations (i.e., $N_T < 250$ m⁻³) occurs frequently in the four seasons in Mèdog.

However, taking the contributor to rainfall into account, drops with $1 \leq D_m < 2$ mm are the largest contributor in the four seasons, and the weak rainfall with $R < 1$ mm h⁻¹ is the largest contributor in Mèdog except during the monsoon season, during which, rainfall with $2 \leq R < 5$ mm h⁻¹ is the largest contributor. For the average spectrum of the four seasons, the monsoon season precipitation has the narrowest spectrum width and is characterized by the highest (lowest) concentration of small (large) drops. The winter (postmonsoon) precipitation has the lowest (highest) concentration of small (large) drops. In terms of rain rate classes, a higher (lower) concentration of small (large) raindrops can be found in the monsoon season for all the considered rainfall rate classes in this study. More large drops and fewer small drops are observed in winter precipitation with $R < 5$ mm h⁻¹. For heavy rainfall (i.e., $R > 5$ mm h⁻¹), the premonsoon precipitation exhibits a higher concentration of large drops.

(2) Mèdog stratiform precipitation in the four seasons has a similar mean D_m value of approximately 1.0 mm but exhibits a distinct difference in the mean value of $\log_{10}(N_w)$. Monsoon stratiform rain has the highest mean $\log_{10}(N_w)$ value of 3.75, followed by postmonsoon rain, and the winter season has the lowest mean $\log_{10}(N_w)$ value of 3.28. The convective rainfall during the monsoon season is characterized by the highest concentration of limited-size drops and is identified as maritime-like. Premonsoon convective rain has predominantly larger drops than other seasons. The largest mean D_m (1.67 mm) and the lowest mean $\log_{10}(N_w)$ (3.70) are observed in the premonsoon convective rainfall, which could be considered a transition between maritime-like and continental-like conditions.

(3) The relationships of μ - Λ and Z - R corresponding to different seasons were also fitted. The μ - Λ relationships of the different periods show little discrepancy. The fitted Z - R relationships for stratiform precipitation exhibit little seasonal variation, and winter stratiform rain has a larger coefficient A and exponent b . The fitted Z - R relationships for convective precipitation show evident discrepancies among the premonsoon, monsoon, and postmonsoon periods. The Z - R relationship in monsoon convective rainfall has a smaller (larger) coefficient A (exponent b) than in other seasons, indicating a higher rain rate in monsoon convective precipitation for a given radar reflectivity. The empirical relationship of $Z = 300R^{1.4}$ at midlatitudes would cause the severe underestimation of convective rain in Mèdog, especially during the monsoon period.

(4) The possible causative meteorological environments responsible for the seasonal variation in DSDs in Mèdog were discussed. Westerlies prevail over the whole TP in the premonsoon season, and rainfall is dominated by cold rain processes, resulting in the formation of large raindrops via the melting of frozen particles. In addition, less water vapor and a larger wind speed contribute to stronger evaporation, which probably leads to a lower concentration of small drops in the premonsoon precipitation. During the monsoon period, abundant warm and humid mass air intrudes from the Indian Ocean into Mèdog, and warm rain processes prevail in this period, producing many small raindrops via active collision and coalescence processes. Atmospheric conditions are characterized by humid and weak winds in the postmonsoon season, which is favorable to the production of small drops.

Notably, this work focused on the seasonal variation in DSD based on disdrometer data in Mèdog. The parameters of gamma distribution model of DSDs are trying to be used to improve the microphysical parameterization scheme of precipitation in the local numerical model. The detailed performance of the model will be evaluated later. Furthermore, disdrometer observations at more locations over the TP will be used to explore the temporal and spatial variation in DSDs. In addition, the vertical structure of DSDs in different seasons will be explored in future research by jointly using K-band Micro Rain Radar and X-band dual-polarization radar observations.

Author Contributions: Conceptualization, G.W. and L.L.; methodology, R.L. and G.W.; software, R.L., R.Z. and J.Z.; writing—original draft preparation, R.L.; writing—review and editing, R.L., G.W.; funding acquisition, G.W. All authors have read and agreed to the published version of the manuscript.

Funding: This project was funded by the Second Tibetan Plateau Scientific Expedition and Research (STEP) program, grant number 2019QZKK0105 and the National Key R & D Projects, grant number 2018YFC1505702.

Acknowledgments: We thank Suolang Zhaxi and Ting Wang for their help in the maintenance of the disdrometer at Mêdog National Climate Observatory.

Conflicts of Interest: The authors declare no conflict of interest.

References

- Seela, B.K.; Janapati, J.; Lin, P.-L.; Reddy, K.K.; Shirooka, R.; Wang, P.K. A Comparison Study of Summer Season Raindrop Size Distribution Between Palau and Taiwan, Two Islands in Western Pacific. *J. Geophys. Res. Atmos.* **2017**, *122*, 11787–11805. [[CrossRef](#)]
- Han, Y.; Guo, J.; Yun, Y.; Li, J.; Guo, X.; Lv, Y.; Wang, D.; Li, L.; Zhang, Y. Regional variability of summertime raindrop size distribution from a network of disdrometers in Beijing. *Atmos. Res.* **2021**, *257*, 105591. [[CrossRef](#)]
- Sreekanth, T.S.; Varikoden, H.; Sukumar, N.; Mohan Kumar, G. Microphysical characteristics of rainfall during different seasons over a coastal tropical station using disdrometer. *Hydrol. Process.* **2017**, *31*, 2556–2565. [[CrossRef](#)]
- Tang, Q.; Xiao, H.; Guo, C.; Feng, L. Characteristics of the raindrop size distributions and their retrieved polarimetric radar parameters in northern and southern China. *Atmos. Res.* **2014**, *135–136*, 59–75. [[CrossRef](#)]
- Thompson, E.J.; Rutledge, S.A.; Dolan, B.; Thurai, M. Drop Size Distributions and Radar Observations of Convective and Stratiform Rain over the Equatorial Indian and West Pacific Oceans. *J. Atmos. Sci.* **2015**, *72*, 4091–4125. [[CrossRef](#)]
- Krishna, U.V.M.; Reddy, K.K.; Seela, B.K.; Shirooka, R.; Lin, P.-L.; Pan, C.-J. Raindrop size distribution of easterly and westerly monsoon precipitation observed over Palau islands in the Western Pacific Ocean. *Atmos. Res.* **2016**, *174–175*, 41–51. [[CrossRef](#)]
- Löffler-Mang, M.; Joss, J. An Optical Disdrometer for Measuring Size and Velocity of Hydrometeors. *J. Atmos. Ocean. Technol.* **2000**, *17*, 130–139. [[CrossRef](#)]
- Nzeukou, A.; Sauvageot, H.; Ochou, A.D.; Kebe, C.M. Raindrop Size Distribution and Radar Parameters at Cape Verde. *J. Appl. Meteorol. Climatol.* **2004**, *43*, 90–105. [[CrossRef](#)]
- Lavanya, S.; Kirankumar, N.V.P. Classification of tropical coastal precipitating cloud systems using disdrometer observations over Thumba, India. *Atmos. Res.* **2021**, *253*, 105477. [[CrossRef](#)]
- Huo, Z.; Ruan, Z.; Wei, M.; Ge, R.; Li, F.; Ruan, Y. Statistical characteristics of raindrop size distribution in south China summer based on the vertical structure derived from VPR-CFMCW. *Atmos. Res.* **2019**, *222*, 47–61. [[CrossRef](#)]
- Radhakrishna, B.; Rao, T.N.; Rao, D.N.; Rao, N.P.; Nakamura, K.; Sharma, A.K. Spatial and seasonal variability of raindrop size distributions in southeast India. *J. Geophys. Res.* **2009**, *114*, D04203. [[CrossRef](#)]
- Pu, K.; Liu, X.; Wu, Y.; Hu, S.; Liu, L.; Gao, T. A comparison study of raindrop size distribution among five sites at the urban scale during the East Asian rainy season. *J. Hydrol.* **2020**, *590*, 125500. [[CrossRef](#)]
- Wu, Z.; Zhang, Y.; Zhang, L.; Lei, H.; Xie, Y.; Wen, L.; Yang, J. Characteristics of Summer Season Raindrop Size Distribution in Three Typical Regions of Western Pacific. *J. Geophys. Res. Atmos.* **2019**, *124*, 4054–4073. [[CrossRef](#)]
- Hopper, L.J.; Schumacher, C.; Humes, K.; Funk, A. Drop-Size Distribution Variations Associated with Different Storm Types in Southeast Texas. *Atmosphere* **2019**, *11*, 8. [[CrossRef](#)]
- Chen, B.; Hu, Z.; Liu, L.; Zhang, G. Raindrop Size Distribution Measurements at 4,500 m on the Tibetan Plateau During TIPEX-III. *J. Geophys. Res. Atmos.* **2017**, *122*, 11092–11106. [[CrossRef](#)]
- Wu, Y.; Liu, L. Statistical characteristics of raindrop size distribution in the Tibetan Plateau and southern China. *Adv. Atmos. Sci.* **2017**, *34*, 727–736. [[CrossRef](#)]
- Zeng, Y.; Yang, L.; Tong, Z.; Jiang, Y.; Zhang, Z.; Zhang, J.; Zhou, Y.; Li, J.; Liu, F.; Liu, J.; et al. Statistical Characteristics of Raindrop Size Distribution during Rainy Seasons in Northwest China. *Adv. Meteorol.* **2021**, *2021*, 6667786. [[CrossRef](#)]
- Zeng, Q.; Zhang, Y.; Lei, H.; Xie, Y.; Gao, T.; Zhang, L.; Wang, C.; Huang, Y. Microphysical Characteristics of Precipitation during Pre-monsoon, Monsoon, and Post-monsoon Periods over the South China Sea. *Adv. Atmos. Sci.* **2019**, *36*, 1103–1120. [[CrossRef](#)]
- Gao, Y.; Zhou, X.; Wang, Q.; Wang, C.; Zhan, Z.; Chen, L.; Yan, J.; Qu, R. Vegetation net primary productivity and its response to climate change during 2001–2008 in the Tibetan Plateau. *Sci. Total Environ.* **2013**, *444*, 356–362. [[CrossRef](#)]
- Zhang, W.; Zhang, L.; Zhou, T. Interannual Variability and the Underlying Mechanism of Summer Precipitation over the Yarlung Zangbo River Basin. *Chin. J. Atmos. Sci.* **2016**, *40*, 965–980. (In Chinese) [[CrossRef](#)]
- Gao, D. Expeditionary studies on the Moisture Passage of the Yarlung Zangbo River. *Chin. J. Nat.* **2008**, *5*, 301–303. (In Chinese)
- Wang, J.; De, Q.; Dan, Z.; Wang, Y.; De, J.; Chen, G.; Tian, Y. Characteristic and Causal Analysis of Concentrated and Frequently Occurring Intense Rainfall in Tibet in 2012–2018. *Meteorol. Sci. Technol.* **2021**, *49*, 211–217.
- Zhou, R.; Wang, G.; Zhaxi, S. Cloud vertical structure measurements from a ground-based cloud radar over the southeastern Tibetan Plateau. *Atmos. Res.* **2021**, *258*, 211–217. (In Chinese) [[CrossRef](#)]
- Wang, G.; Zhou, R.; Zhaxi, S.; Liu, S. Raindrop size distribution measurements on the Southeast Tibetan Plateau during the STEP project. *Atmos. Res.* **2021**, *249*, 105311. [[CrossRef](#)]
- Yuter, S.E.; Kingsmill, D.E.; Nance, L.B.; Löffler-Mang, M. Observations of Precipitation Size and Fall Speed Characteristics within Coexisting Rain and Wet Snow. *J. Appl. Meteorol. Climatol.* **2006**, *45*, 1450–1464. [[CrossRef](#)]

26. Thurai, M.; Petersen, W.A.; Tokay, A.; Schultz, C.; Gatlin, P. Drop size distribution comparisons between Parsivel and 2-D video disdrometers. *Adv. Geosci.* **2011**, *30*, 3–9. [[CrossRef](#)]
27. Beard, K.V. Terminal Velocity and Shape of Cloud and Precipitation Drops Aloft. *J. Atmos. Sci.* **1976**, *33*, 851–864. [[CrossRef](#)]
28. Atlas, D.; Srivastava, R.; Sekhon, R. Doppler Radar Characteristics of Precipitation at Vertical Incidence. *Rev. Geophys. Space Phys.* **1973**, *11*, 1–35. [[CrossRef](#)]
29. Wen, L.; Zhao, K.; Zhang, G.; Liu, S.; Chen, G. Impacts of Instrument Limitations on Estimated Raindrop Size Distribution, Radar Parameters, and Model Microphysics during Mei-Yu Season in East China. *J. Atmos. Ocean. Technol.* **2017**, *34*, 1021–1037. [[CrossRef](#)]
30. Ulbrich, C.W.; Atlas, D. Rainfall Microphysics and Radar Properties: Analysis Methods for Drop Size Spectra. *J. Appl. Meteorol. Climatol.* **1998**, *37*, 912–923. [[CrossRef](#)]
31. Kozu, T.; Nakamura, K.J.J.A.O.T. Rainfall Parameter Estimation from Dual-Radar Measurements Combining Reflectivity Profile and Path-integrated Attenuation. *J. Atmos. Ocean. Technol.* **1991**, *8*, 259–270. [[CrossRef](#)]
32. Testud, J.; Oury, S.; Black, R.A.; Amayenc, P.; Dou, X. The Concept of “Normalized” Distribution to Describe Raindrop Spectra: A Tool for Cloud Physics and Cloud Remote Sensing. *J. Appl. Meteorol.* **2001**, *40*, 1118–1140. [[CrossRef](#)]
33. Smith, P.L. Raindrop Size Distributions: Exponential or Gamma—Does the Difference Matter? *J. Appl. Meteorol.* **2003**, *42*, 1031–1034. [[CrossRef](#)]
34. Bringi, V.N.; Chandrasekar, V.; Hubbert, J.; Gorgucci, E.; Randeu, W.L.; Schoenhuber, M. Raindrop Size Distribution in Different Climatic Regimes from Disdrometer and Dual-Polarized Radar Analysis. *J. Atmos. Sci.* **2003**, *60*, 354–365. [[CrossRef](#)]
35. Steiner, M.; Waldvogel, A. Peaks in Raindrop Size Distributions. *J. Atmos. Sci.* **1987**, *44*, 3127–3134. [[CrossRef](#)]
36. Tokay, A.; Short, D.A. Evidence from Tropical Raindrop Spectra of the Origin of Rain from Stratiform versus Convective Clouds. *J. Appl. Meteorol. Climatol.* **1996**, *35*, 355–371. [[CrossRef](#)]
37. Wang, G.; Li, R.; Sun, J.; Xu, X.; Zhou, R.; Liu, L. Comparative Analysis of the Characteristics of Rainy Season Raindrop Size Distributions in Two Typical Regions of the Tibetan Plateau. *Adv. Atmos. Sci.* **2022**, *39*, 1062–1078. [[CrossRef](#)]
38. Zhang, G.; Vivekanandan, J.; Brandes, E.A.; Meneghini, R.; Kozu, T. The Shape–Slope Relation in Observed Gamma Raindrop Size Distributions: Statistical Error or Useful Information? *J. Atmos. Ocean. Technol.* **2003**, *20*, 1106–1119. [[CrossRef](#)]
39. Wen, L.; Zhao, K.; Wang, M.; Zhang, G. Seasonal Variations of Observed Raindrop Size Distribution in East China. *Adv. Atmos. Sci.* **2019**, *36*, 346–362. [[CrossRef](#)]
40. Luo, L.; Guo, J.; Chen, H.; Yang, M.; Chen, M.; Xiao, H.; Ma, J.; Li, S. Microphysical Characteristics of Rainfall Observed by a 2DVD Disdrometer during Different Seasons in Beijing, China. *Remote Sens.* **2021**, *13*, 2303. [[CrossRef](#)]
41. Chen, B.; Yang, J.; Gao, R.; Zhu, K.; Zou, C.; Gong, Y.; Zhang, R. Vertical Variability of the Raindrop Size Distribution in Typhoons Observed at the Shenzhen 356-m Meteorological Tower. *J. Atmos. Sci.* **2020**, *77*, 4171–4187. [[CrossRef](#)]
42. Rosenfeld, D.; Ulbrich, C.W. Cloud Microphysical Properties, Processes, and Rainfall Estimation Opportunities. *Meteorol. Monogr.* **2003**, *30*, 237–258. [[CrossRef](#)]
43. Fulton, R.A.; Breidenbach, J.P.; Seo, D.-J.; Miller, D.A.; O’Bannon, T. The WSR-88D Rainfall Algorithm. *Weather Forecast.* **1998**, *13*, 377–395. [[CrossRef](#)]
44. Marshall, J.; Palmer, W. The Distribution of Raindrops with Size. *J. Atmos. Sci.* **1948**, *5*, 165–166. [[CrossRef](#)]
45. Zhang, G.; Vivekanandan, J.; Brandes, E. A method for estimating rain rate and drop size distribution from polarimetric radar measurements. *IEEE Trans. Geosci. Remote Sens.* **2001**, *39*, 830–841. [[CrossRef](#)]
46. Barber, P.; Yeh, C. Scattering of electromagnetic waves by arbitrarily shaped dielectric bodies. *Appl. Opt.* **1975**, *14*, 2864–2872. [[CrossRef](#)]
47. Barnes, S.L. An Empirical Shortcut to the Calculation of Temperature and Pressure at the Lifted Condensation Level. *J. Appl. Meteorol. Climatol.* **1968**, *7*, 511. [[CrossRef](#)]
48. McVicar, T.R.; Roderick, M.L.; Donohue, R.J.; Li, L.T.; Van Niel, T.G.; Thomas, A.; Grieser, J.; Jhajharia, D.; Himri, Y.; Mahowald, N.M.; et al. Global review and synthesis of trends in observed terrestrial near-surface wind speeds: Implications for evaporation. *J. Hydrol.* **2012**, *416–417*, 182–205. [[CrossRef](#)]
49. Dolan, B.; Fuchs, B.; Rutledge, S.A.; Barnes, E.A.; Thompson, E.J. Primary Modes of Global Drop Size Distributions. *J. Atmos. Sci.* **2018**, *75*, 1453–1476. [[CrossRef](#)]
50. Maddox, R.A. Mesoscale convective complexes. *Bull. Am. Meteorol. Soc.* **1980**, *61*, 1374–1387. [[CrossRef](#)]
51. Fujinami, H.; Yasunari, T. The Seasonal and Intraseasonal Variability of Diurnal Cloud Activity over the Tibetan Plateau. *J. Meteorol. Soc. Jpn. Ser. II* **2001**, *79*, 1207–1227. [[CrossRef](#)]